Neutron transition densities for ^{48}Ca from proton scattering at 200 and 318 MeV

A. E. Feldman,* J. J. Kelly, B. S. Flanders,† M. A. Khandaker,‡ H. Seifert,§ P. Boberg,‖ and S. D. Hyman¶
Department of Physics, University of Maryland, College Park, Maryland 20742

P. H. Karen, B. E. Norum, and P. Welch**
Department of Physics, University of Virginia, Charlottesville, Virginia 22901

Q. Chen,†† A. D. Bacher, G. P. A. Berg, and E. J. Stephenson
Department of Physics, Indiana University, Bloomington, Indiana 47401

S. Nanda and A. Saha
Continuous Electron Beam Accelerator Facility, Newport News, Virginia 23606

A. Scott
Department of Physics and Astronomy, University of Georgia, Athens, Georgia 30602
(Received 10 November 1993)

Differential cross sections and analyzing powers for scattering of 200 and 318 MeV protons have been measured for states of ^{48}Ca up to 7 MeV of excitation. The data cover c.m. momentum transfers from approximately 0.4 to 3.0 fm^{-1}. Neutron transition densities were extracted for the 2_1^+, 3_1^-, 3_2^-, 4_2^+, and 5_1^- states using density-dependent empirical effective interactions previously calibrated upon elastic and inelastic scattering data for ^{16}O and ^{40}Ca. The corresponding proton transition densities were obtained from electron scattering data and held fixed during the analysis. Fits performed to the data for either energy provide excellent predictions for the other. Neutron densities fitted to data for either energy independently agree very well with each other and with the densities fitted to both data sets simultaneously. These densities are also consistent with earlier data for 500 MeV protons. The energy independence of the extracted transition densities demonstrates that residual errors in the reaction model are compatible with the error bands estimated by the fitting procedure. Several additional tests of the model dependence of the results were performed also. The proton and neutron transition densities are compared with calculations based upon the extended random phase approximation, which includes $2p2h$ correlations. These calculations are most successful for densities dominated by $1p1h$ configurations, whereas densities requiring substantial $2p2h$ contributions tend to be underestimated.

PACS number(s): 27.40.+z, 25.40.Ep, 25.40.Cm, 21.60.Jz

I. INTRODUCTION

We have measured cross sections and analyzing powers for elastic and inelastic scattering of 200 and 318 MeV protons by ^{48}Ca and have deduced neutron transition densities for several normal-parity excitations. Proton transition densities for these states were previously measured with electron scattering [1] and were used in the analysis of these proton scattering data. Electron and proton scattering data for ^{42,44}Ca have also been acquired [2] and will be reported in future publications. The present work is part of a program whose primary purpose is to study the evolution of neutron and proton transition densities for the calcium isotopes as the $1f_{7/2}$ neutron shell is filled. We begin with the doubly magic ^{48}Ca nucleus, for which extensive nuclear structure calculations are available. Most notably, the recent calculations of Brand *et al.* [3,4] using the extended random phase approximation (ERPA) to include $2p2h$ correlations have enjoyed considerable success in describing the electron scattering data for ^{48}Ca. These calculations predict significant differences between proton and neutron densities.

Comparisons between predicted and measured transition densities can provide considerable insight into the evaluation of nuclear structure theories. Proton transi-

*Present address: Department of Physics, Ohio University, Athens, OH 45701.
†Present address: Department of Physics, The American University, Washington, D.C. 20016.
‡Present address: Physics Dept., LEGS Group, Brookhaven National Lab, Upton, NY 11973.
§Present address: Code 661, NASA-Goddard Space Flight Center, Greenbelt, MD 20771.
‖Present address: Naval Research Laboratory, Code 7654, Washington, D.C. 20375.
¶Present address: Dept. of Physics, Sweet Briar College, Sweet Briar, VA 24595.
**Present address: Department of Physics, Massachusetts Institute of Technology, Cambridge, MA 02139.
††Present address: Department of Physics, Beijing University, People's Republic of China.

tion densities are readily and accurately measured using high-energy electron scattering [5,6], but most previous attempts to measure neutron transition densities via hadronic scattering data have been greatly hindered by uncertainties in both the reaction mechanism and the effective interaction. Thus, whereas most of these analyses were content to extract a simple scale factor which characterizes the relative contributions of neutrons and protons in a qualitative manner [7–9], radial densities provide much more detailed information and more rigorous tests of structure theories [10–16].

It has been shown that proton scattering is capable of determining neutron transition densities with good radial sensitivity provided that the effective interaction is known with adequate accuracy [10]. Consequently, we have developed methods for fitting neutron transition densities to nucleon scattering data that are similar to the nearly model-independent analysis procedures used for electron scattering data. This procedure, called the linear expansion analysis (LEA) method, has been described in detail in previous papers [10,15,13,14] and has been applied to extract neutron transition densities from (p,p') data for ^{18}O [11], ^{30}Si [12], ^{34}S [14], and ^{88}Sr [16]. The error analysis used in our method includes contributions due to penetrability, the statistical and normalization uncertainties in the data, and the uncertainty due to the finite range of momentum transfer that is measured. These uncertainties are combined to produce error envelopes which depend upon radius. While this procedure provides estimates of the precision of the extracted densities, determination of their accuracy requires much more care: Residual errors in the reaction model are not represented in the error envelope.

However, since theoretical nuclear-matter interactions are not yet sufficiently accurate for this purpose, it is necessary to employ empirical effective interactions calibrated to data for which the transition densities are known accurately [17,18]. The starting point for obtaining these empirical interactions is to make a parametrization that can be fitted to nuclear matter interactions. Then, the parameters are optimized by fitting to a large body of (p,p') data for transitions whose relevant nuclear structure is independently known from electron scattering. The isoscalar spin-independent central and isoscalar spin-orbit interactions are fitted to normal-parity isoscalar excitations of self-conjugate nuclei. The proton transition densities are obtained from electron scattering and we assume that neutron and proton transition densities are very nearly equal for self-conjugate targets. These interactions provide excellent descriptions of the (p,p') data for $N = Z$ targets and can be used to fit neutron densities to (p,p') data for targets with $N \neq Z$, provided that the proton transition densities are already available from (e,e'). Even when the neutron and proton densities are significantly different, the isoscalar interaction usually still dominates the cross section. Thus, we assume that medium modifications to the isovector interaction are known well enough from nuclear matter theory that residual errors in this small contribution do not compromise the accuracy of the fitted neutron densities.

Several methods for testing the accuracy of the analysis procedures for neutron transition densities are available. The first method to be applied systematically is called the *self-conjugacy test*, in which isoscalar transition densities are fitted to data for self-conjugate targets and compared with proton transition densities from electron scattering. Alternatively, the proton transition density can be supplied and the neutron transition density fitted to data for self-conjugate targets. In either case, we should find $\rho_n(r) = \rho_p(r)$. This method was applied by Kelly *et al.* to data for ^{32}S(p,p') at $E_p = 318$ MeV [13], using interactions fitted to data for ^{16}O and ^{40}Ca, and very good agreement with electron scattering densities was obtained for this target with mass intermediate between those for which the interaction was calibrated. Similar tests for ^{40}Ca using 200 MeV protons [15] were also successful.

Another important test of the accuracy of fitted densities which can applied for $N \neq Z$ targets is based on the requirement that the transition densities, which are properties of the target but not the probe, be independent of the properties of the probe. The neutron transition densities presented in this paper were fitted to data taken with protons of two distinct energies—200 and 318 MeV — and we find that the results are energy independent. Although the properties of the effective interactions at these two energies and the resulting angular distributions are significantly different, the neutron densities fitted to the two data sets are essentially the same. We also find that the fitted densities provide good predictions for data with $E_p = 500$ MeV. Therefore, the accuracy of the fitted densities has been shown to be commensurate with the estimated error envelopes.

In Sec. II we describe the experiment and in Sec. III we summarize our analysis procedures. The sensitivity of fitted densities to uncertainties in the reaction model is discussed in Sec. IV. In Sec. V we present our results for neutron transities in ^{48}Ca and show that they are very nearly independent of energy. Comparisons to previous experiments and to structure calculations are made in Sec. VI and Sec. VII, respectively. Finally, in Sec. VIII we summarize and discuss our conclusions.

II. EXPERIMENT

The acquisition and analysis of the experimental data are described in detail in Ref. [15] for 318 MeV and in Refs. [19,20] for 200 MeV. Brief summaries of these experiments are given here. Data tables for both experiments are on deposit with the Physics Auxiliary Publication Service (PAPS) [21] for the states listed in Table I, where the excitation energies are taken from Ref. [22] and multipolarity assignments from Ref. [23]. These tables include data for many states of ^{48}Ca below 7 MeV excitation not considered in the present paper. Although the data are as complete for many of the states not discussed in this paper as for the states that are, the data for several of the weaker transitions, particularly at 318 MeV, are relatively sparse, as indicated by the comments in Table I.

TABLE I. States of ^{48}Ca up to 7 MeV. Excitation energies are from Ref. [22]. Multipolarity assignments are from Ref. [23]; uncertain assignments are enclosed by parentheses.

E (MeV)	J^π_n	Comments
0.000	0^+_1	
3.832	2^+_1	ρ_n fitted
4.284	0^+_2	
4.503	4^+_1	not resolved from 3^-_1 [a]
4.507	3^-_1	ρ_n fitted
4.612	3^+_1	
5.147	5^+_1	
5.252	(5^+)	sparse 318 MeV data
5.304	(1^-)	sparse 318 MeV data
5.322		sparse data
5.369	3^-_2	ρ_n fitted
5.461	0^+_3	
5.729	5^-_1	ρ_n fitted
6.104	4^-_1	
6.342	4^+_2	ρ_n fitted
6.614	(1^-)	sparse 318 MeV data
6.648	4^+_3	sparse 318 MeV data
6.685	2^-_1	
6.750		sparse data
6.795	2^+	
6.820		sparse 318 MeV data
6.895		sparse 318 MeV data

[a]Data not reported for this state. See Sec. V A 2.

A. 318 MeV experiment

Polarized-proton beams with energies in the range 317.8 ± 0.3 MeV were provided by the Los Alamos Meson Physics Facility (LAMPF). The beam current measured by the ionization chambers was normalized by measuring elastic p-p scattering from a CH_2 target and comparing to phase-shift calculations [24]. The beam polarization was measured by the continuous in-line polarimeter described in Ref. [25] and ranged from about 0.7 to 0.8. The scattered protons were analyzed with the HRS spectrometer using the standard focal-plane array described in Ref. [26]. Data were collected for laboratory scattering angles between 5° and 39° in steps of 2°, plus an additional setting of 9.6°. Spectra were constructed for an acceptance of ±1.03° and were analyzed with the line-shape fitting code ALLFIT [27]. The resolution [full width at half maximum (FWHM)] for the ^{48}Ca peaks varied from about 35 keV for the smallest laboratory angles to about 55 keV for the largest. A typical spectrum is shown in Fig. 1.

The isotopically enriched ^{48}Ca target had a thickness of 7.0 mg/cm^2. By comparing yields extracted for ^{40}Ca peaks to the ^{40}Ca data from Ref. [28], it was determined that the ^{40}Ca contamination in the ^{48}Ca target was 2.2% (stoichiometric percentage). Where the ^{40}Ca peaks were not strong and resolved, the areas of those peaks were held fixed to values consistent with the data from the same reference.

B. 200 MeV experiment

Polarized-proton beams with energies in the range 201.4 ± 0.2 MeV were provided by the Indiana University Cyclotron Facility (IUCF). The accumulated beam charge was measured with Faraday cups internal (external) to the scattering chamber for angles less (greater) than 18°. The small internal cups were calibrated against the larger and more accurate external Faraday cup. The beam polarization was determined from the asymmetry of low-energy proton scattering from ^{4}He using a gas cell lowered into the beam between the injector and main-stage cyclotrons every few hours. Typically polarizations of 72–77% for spin up and 74–79% for spin down were obtained with very little change between measurements.

The ^{48}Ca target had a thickness of 15.2(2) mg/cm^2 and was 97.69(5)% pure. Measurements were made with the K600 spectrometer for laboratory scattering angles

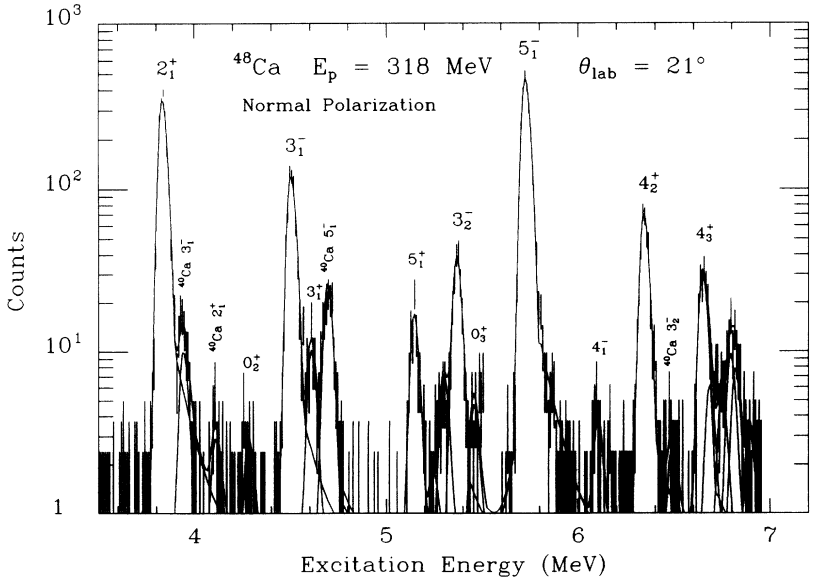

FIG. 1. Typical spectrum for ^{48}Ca(p,p') at E_p = 318 MeV acquired with the HRS spectrometer at LAMPF. Note the logarithmic scale. The total fit and each individual peak are shown, including those due to the small ^{40}Ca impurity.

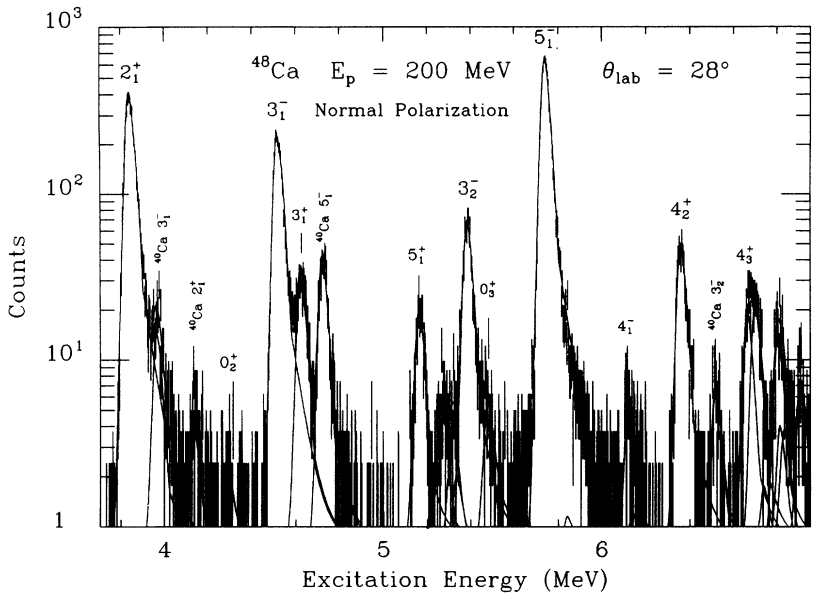

FIG. 2. Typical spectrum for ^{48}Ca(p,p') at E_p = 200 MeV acquired with the K600 spectrometer at IUCF. Note the logarithmic scale. The total fit and each individual peak are shown, including those due to the small ^{40}Ca impurity.

ranging from about 5.86° to 55.27°. The fitting of the spectra was done using the same methods as for the 318 MeV data. A typical spectrum is shown in Fig. 2. The energy resolution was typically 30–50 keV FWHM.

III. ANALYSIS PROCEDURES

A. Folding model

Detailed discussions of our implementation of the folding model and the local density approximation can be found in Refs. [17] and [18]. The methods used for fitting neutron transition densities to proton scattering data can be found in Refs. [10,13–15]. In this section we summarize those aspects of the model relevant to this paper.

Proton scattering calculations were performed with the code LEA [29]. The effective interaction is evaluated for the local density at the projectile site. Knock-on exchange is included in the zero-range approximation [30]. Both optical potentials and scattering potentials were generated from the same effective interactions, except that the density dependence of the inelastic interaction is enhanced with respect to the elastic interaction by the rearrangement factor derived by Cheon *et al.* [31].

All calculations presented here are based upon empirical effective interactions fitted to proton scattering data for both ^{16}O and ^{40}Ca simultaneously [32,28,20]. These analyses fit density-dependent modifications to the isoscalar spin-independent central and spin-orbit components of the nucleon-nucleon effective interaction. However, several analyses have been performed for both energies with different selections of data and different representations of the low-density limit of the effective interaction. For example, slightly different results are obtained when fitting to inelastic data for both targets or when including the elastic data also. Similarly, slightly different results are obtained when the Franey-Love (FL) parametrization of the nucleon-nucleon t matrix [33] is used to represent the free interaction or when the free interaction is taken from the low-density limit of a nuclear matter calculation, such as the Paris-Hamburg (PH) G matrix [34,35]. The latter does not reduce to the nucleon-nucleon t matrix in the limit $k_F \rightarrow 0$. Since it is fitted to nucleon-nucleon data and is available over a broader range of energy, we have chosen to employ empirical effective interactions based upon the FL t matrix. Finally, at each energy we chose the interaction which gives the best results for the self-conjugacy test, which at 200 MeV was found to be the interaction labeled LR3 in Table II of Ref. [20] and at 318 MeV the interaction labeled EI3 in Table I of Ref. [28]. The former includes both elastic and inelastic data, whereas the latter is based upon inelastic scattering data only. We found that use of the 318 MeV interaction that includes the elastic data gave slightly inferior self-conjugacy results to the interaction based upon inelastic scattering data alone, possibly because the density dependence of the 318 MeV interaction is so strong that minor inaccuracies in the Cheon rearrangement prescription could adversely affect the interaction fitted to elastic and inelastic scattering simultaneously. At 200 MeV, on the other hand, exclusion of the elastic data from the analysis of the effective interaction has very little effect upon the ^{48}Ca analysis.

For both energies the isovector components of the effective interaction were obtained by parametrizing the density dependence of the theoretical effective interaction due to Ray [36] and applying the corrections to the FL t matrix as described in Ref. [32]. This model of the effective interaction is designated LR. The sensitivity of the fitted neutron densities to ambiguities in these prescriptions is examined in Sec. IV and is found to be small.

Proton transition densities were obtained by unfolding the proton form factor from the transition charge densities measured by Wise *et al.* [1] using electron scattering and were not varied during the analysis. Similarly, the ground-state proton density was obtained by unfolding

the proton form factor from the charge density tabulated in Ref. [37]. Predictions for proton elastic scattering from ^{48}Ca at 200 MeV and 318 MeV are compared with data in Fig. 3, where the solid lines are based upon the assumption $\rho_n \propto \rho_p$ and the dashed lines employ ground-state neutron densities constructed by Ray [38] by adding a theoretical model of $\rho_n - \rho_p$ to the measured ρ_p. Although the latter provides a slightly better description of the elastic scattering data for intermediate momentum transfers, the differences between neutron transition densities fitted to inelastic scattering data using distorted waves based upon these two models are extremely small because distortion of inelastic scattering is quite insensitive to details of the ground-state neutron density [15]. Therefore, the fits for inelastic scattering were performed assuming proportionality between the ground-state neutron and proton densities, which should not cause any significant errors in the fitted densities. Furthermore, the small discrepancies between the elastic data and the calculations at large momentum transfers should have a negligible effect on inelastic scattering.

B. Transition densities

The matter densities are defined by

$$\rho_{J\tau}(r) = \sum_i \langle f || \frac{\delta(r - r_i)}{r^2} Y_J(\hat{r}_i) || i \rangle, \tag{1}$$

where the sum runs over either protons or neutrons when

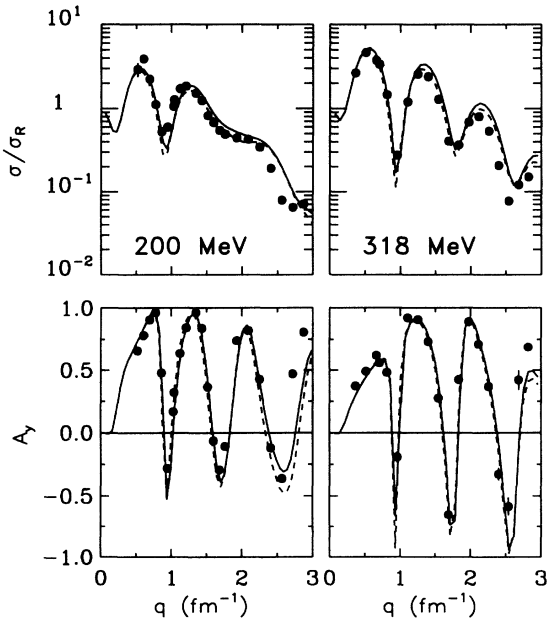

FIG. 3. Data for elastic scattering of 200 and 318 MeV protons by ^{48}Ca are compared with calculations based upon the empirical effective interactions for those energies. The solid curves use the proton density from electron scattering and assume $\rho_n \propto \rho_p$. The dashed curves use a neutron transition density based upon a theoretical calculation of $\rho_n - \rho_p$, as described in the text.

$\tau = p$ or n, respectively. It is also convenient to define isoscalar and isovector densities $\rho_0 = \rho_n + \rho_p$ and $\rho_1 = \rho_n - \rho_p$, respectively. Although it is customary to represent the proton density as a Fourier-Bessel expansion (FBE) when analyzing electron scattering data, we find it more convenient to represent neutron densities using the Laguerre-Gaussian expansion (LGE) when analyzing proton scattering data. Hence, we expand the density

$$\rho_J(r) = x^J e^{-x^2} \sum_n a_n L_n^{J+1/2}(2x^2), \tag{2}$$

where $x = r/b$ is a radial variable scaled by the oscillator parameter b and L_n^ν is a generalized Laguerre polynomial of order n. We have chosen to use $b = 2.0$ fm for the calcium isotopes based upon the harmonic-oscillator shell model.

The strength of the transition is customarily characterized by the multipole moment or matrix element

$$M_{J\tau}(r) = \int dr\, r^{J+2} \rho_{J\tau}(r), \tag{3}$$

where again $\tau = p$ for protons and n for neutrons. The subscript J will be omitted whenever possible for brevity in the rest of this work. Unfortunately, the moments M_n and M_p are often not determined very well by scattering experiments. These quantities strongly emphasize very large radii through the weighting factor r^{J+2}. Scattering experiments for intermediate momentum transfers, typically $0.25 \leq q \leq 3.0$ fm^{-1}, provide accurate measurements of transition densities for intermediate radii, typically $1 \leq r \leq 8$ fm, but determine neither very long nor very short wavelengths. The analysis of such data requires the use of both high momentum and large radius constraints. However, even when a tail bias is applied with considerable care, imperfections in the data in localized regions of momentum transfer sometimes tend to produce unlikely structures in the fitted densities at large radii. The M_n and M_p values can then depend too strongly on the details of the tail bias. Therefore, long-wavelength quantities such as M_n and M_p cannot be determined in a model-independent fashion.

In order to obtain a relatively model-independent measure of the relative strengths of neutron and proton transition densities, it is useful to employ the ratio

$$R_{np} = \tilde{\rho}_n(q_n)/\tilde{\rho}_p(q_p), \tag{4}$$

where

$$\tilde{\rho}_\lambda(q) = \int dr\, r^2 j_J(qr) \rho_\lambda(r) \tag{5}$$

is the Fourier-Bessel transform of the proton or neutron transition density where $\lambda = p$ or n and where q_λ is the momentum transfer for which $\tilde{\rho}_\lambda$ attains its maximum value. Therefore, since both the numerator and denominator are usually accurately determined by scattering experiments, R_{np} should be stable and subject to little model dependence. In fact, we have found in several previous analyses that variations of the tail bias which

produce as much as 20% variations in M_n result in less than 1% variations in R_{np}. Since R_{np} is based upon the peaks of the form factors, it should more closely represent the results of scaling analyses than does the ratio M_n/M_p.

The moments we quote for proton transition densities were obtained from the electron scattering work of Wise *et al.* [1]. However, inspection of the moment integrand $r^{J+2}\rho_p(r)$ reveals that insufficient attention was paid to the large-r behavior during that analysis, resulting in unrealistically strong oscillations at large radii for some of the densities. Hence, we believe that the uncertainties they quote for M_p are overly optimistic. Fortunately, although errors in M_p can affect the ratio M_n/M_p, the R_{np} ratio is relatively insensitive to the tail of the density and should be more stable. Moreover, even when other authors express their results in the form of M_n/M_p, it is usually a quantity similar to R_{np} that they have obtained by analyzing the peaks of angular distributions.

C. Fitting procedures

A high-q bias is applied to the fits to facilitate estimation of the incompleteness error that results from the limited range of momentum transfer for which data are fitted. Although for most states data are available for larger momentum transfers, the fits were restricted to a range of momentum transfer $q \leq 2.7$ fm^{-1} for several reasons. First, charge form factors tend to be known well only up to about twice the Fermi momentum (which is about 2.7 fm^{-1}). Second, the validity of the reaction model also tends to be limited to values of q up to about twice the Fermi momentum. Finally, it is expected that the form factors drop precipitously after this.

Additional uncertainties of $\pm 5\%$ for cross sections and ± 0.05 for analyzing powers were folded into the data for all the fits. This was done partly to account for residual errors in the reaction model and partly to put approximately equal weighting on the observables throughout the fitted range of momentum transfer. However, all data shown in this work are plotted with the original error bars. Finally, normalization errors of $\pm 5\%$ were assumed for both data sets, 200 and 318 MeV. The contribution of the normalization uncertainty to the error bands was evaluated by refitting the densities using renormalized cross sections. When fits were performed with more than one data set, the normalization errors were evaluated for each data set independently and the contributions to the error bands were combined in quadrature.

An important physical constraint concerns the large-r behavior of the radial density. While higher-order terms allow a more flexible shape, they also permit ringing at unreasonably large r. These unphysical artifacts of fitting a linear expansion can cause very large errors in the determination of moments for which the density is weighted by a large power of r. This error can be minimized through the addition of a penalty function

$$\chi_t^2 = \sum_i \frac{[t(r_i) - \rho(r_i)]^2}{[wt(r_i)]^2} \qquad (6)$$

to χ^2 that inhibits deviations of the fitted density from radial pseudodata that obey the asymptotic tail function

$$t(r) = se^{-dr}/r^n, \qquad (7)$$

where s is matched to $\rho_n(r)$ at $r = r_m$. Although an earlier analysis for ^{30}Si [12] used the above equation with $n = 2$, the results are rather insensitive to the choice of n and subsequent analyses, including the present work, were performed with $n = 0$. Similarly, since the fits to scattering data are relatively insensitive to the value of d, this parameter was chosen by examining the moment integrand $r^{J+2}\rho_n(r)$ for $r > r_m$. We find that the choices $r_m = 7.0$ fm and $d = 3.5$ fm produce smooth tails without large-r oscillations and with very little impact upon fits to the data. Note that these choices are similar to those made previously for ^{88}Sr [16], but lighter nuclei seem to prefer smaller values of d.

For all states except 4_2^+, a tail weight of $w = 1.0$ was sufficient, but for the 4_2^+ data at 200 MeV a stronger tail bias was required. Hence, the 4_2^+ data for both energies were analyzed with $w = 0.1$. For each state ten radial pseudodata spaced by 0.5 fm were employed for the tail bias.

Figure 4 shows a plot of the error envelope for the 2_1^+ state of ^{48}Ca fit to 200 and 318 MeV data simultaneously. The normalization error dominates at large r because of its effect on the low-q data and the M_0 moment. The statistical uncertainties dominate at intermediate values of r because the data cover mainly intermediate values of q. The incompleteness error dominates in the interior where the limitation in the range of momentum transfer has the greatest effect.

IV. SENSITIVITY TO MODELS OF THE EFFECTIVE INTERACTION

The empirical interactions used to fit the neutron densities in this paper have already undergone extensive testing for accuracy and A independence [32,28,20,19]. However, the fitting of densities offers additional important tests.

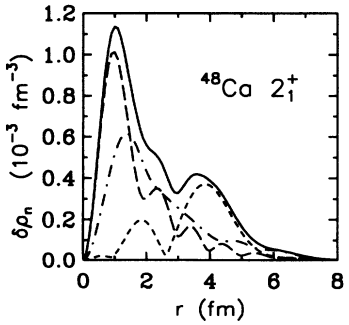

FIG. 4. The error band (solid lines) for the neutron transition density for the 2_1^+ state of ^{48}Ca is decomposed into statistical (dash-dotted lines), incompleteness (long-dashed lines), and normalization (short-dashed lines) contributions.

A. Self-conjugacy tests

An important test of the accuracy of the effective interactions can be made by fitting isoscalar densities to data for self-conjugate targets, such as ^{40}Ca, where charge symmetry ensures that $\rho_n(r)$ and $\rho_p(r)$ are very nearly equal. Thus the isoscalar density $\rho_0 = \rho_n + \rho_p$ can be fit to data for self-conjugate targets without supplying any nuclear structure input. If the interaction is accurate, the resulting isoscalar density should be just twice the point proton density. This procedure, known as the self-conjugacy test, allows us to fit proton transition densities to (p,p') data for comparison to the completely independent and *a priori* more reliable (e,e') proton transition densities.

An analysis of this type was presented by Kelly *et al.* [13] for ^{32}S(p,p') at 318 MeV, where it was demonstrated that isoscalar densities fitted using the empirical effective interaction reproduce electron scattering measurements very well. It was also found that use of the empirical effective interaction was essential to obtaining good agreement between (p,p') and (e,e')— theoretical effective interactions gave much less satisfactory results. A similar analysis of data for 200 MeV protons scattered by ^{40}Ca is presented in Ref. [15], where again good agreement between (p,p') and (e,e') is obtained using empirical interactions and inferior results with theoretical interactions.

In Fig. 5 we compare transition densities fitted to 200 and 318 MeV proton scattering data for ^{40}Ca [20,28] with densities fitted to electron scattering data by Miskimen [39]. Dashed lines were fitted to 200 MeV data, dotted lines to 318 MeV, and solid lines to electron scattering. The error bands fitted to both proton scattering data sets simultaneously encompass the single-energy fits over most of the radial range, demonstrating the energy independence of the fitted densities. The densities fitted to proton scattering data agree very well with those fitted to electron scattering, demonstrating the accuracy of the fitted densities. However, since the analysis of the electron scattering data did not treat the tail bias as carefully as the present analysis of proton scattering, several of the densities from (e,e'), such as the 2_1^+ and 3_2^- densities, exhibit significant large-r oscillations. These oscillations, which are especially evident in plots of $r^{J+2}\rho_p$, are probably correlated with the more pronounced interior structure present in some of the (e,e') densities. Therefore, we do not regard these small differences between the two analyses to be meaningful and consider the self-conjugacy test to have been fully satisfied by the empirical effective interactions chosen for the analysis of the ^{48}Ca data.

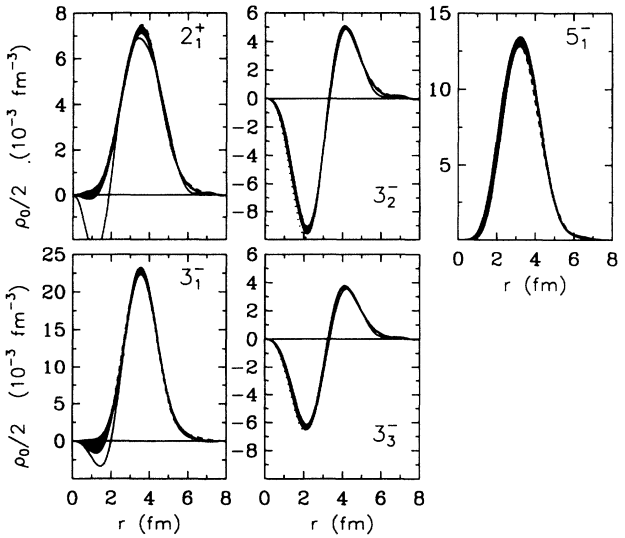

FIG. 5. Self-conjugacy test. Transition densities for ^{40}Ca fitted to proton scattering data for 200 MeV (dashed lines), 318 MeV (dotted lines), or both data sets simultaneously (bands) are compared with densities from electron scattering (solid lines).

B. Dependence upon the isovector interaction

Since the isovector components of the effective interaction are not determined by fits of the empirical effective interaction to isoscalar transitions within self-conjugate nuclei, it is also important to evaluate the effect of possible uncertainties in the isovector interaction upon the fitted neutron densities. Among the states analyzed herein, we find that the isovector density is most important for the 2_1^+ state. Furthermore, the relative strength of the isovector interaction compared with the isoscalar interaction decreases over the energy range considered. Hence, the analysis of the 200 MeV data for the 2_1^+ state should be most sensitive to possible ambiguities in the isovector interaction. Therefore, we refitted these data using several variations of the isovector interaction. First, the empirical interaction based upon the FL t matrix including the LR theory for the density dependence of the isovector interaction was used to extract the neutron transition density. Second, the density dependence of the LR isovector interaction was turned off and the neutron density was refitted. Third, the isovector interaction was eliminated completely and yet another neutron density was fitted.

The results of these three variations are compared in Fig. 6, which shows that the differences between them

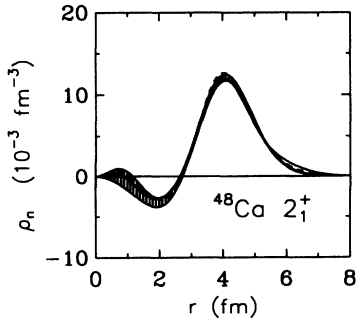

FIG. 6. The sensitivity of ρ_n fitted to the 200 MeV data for the 2_1^+ state of ^{48}Ca to uncertainties in the isovector interaction is illustrated by comparing fits excluding the isovector interaction (solid lines) or using a density-independent isovector interaction (dashed lines) with the full analysis (band).

are very small. Thus, substitution of the low-density limit of the isovector force for the density-dependent version has very little effect and even complete exclusion of the isovector force has relatively little effect on the fitted density. The somewhat larger density near $r \approx 6$ fm that results from elimination of the isovector interaction altogether increases the fitted value of M_n by 9%, which is about 3 times its estimated uncertainty. Since this is an unrealistically large variation of the isovector interaction, the uncertainty in M_n due to the isovector interaction must be smaller. Therefore, the LR isovector terms would have to be grossly inaccurate to have any significant impact on the fitted neutron densities. Furthermore, since the isovector contribution decreases with increasing energy, uncertainties due to the isovector interaction at 318 MeV and 500 MeV should be even less than shown here.

C. Ambiguities in the low-density interaction

Finally we consider the sensitivity of fitted neutron densities to possible ambiguities in the effective interaction for low densities. Although a strict interpretation of the local density approximation (LDA) would require the effective interaction to approach the free nucleon-nucleon t matrix in the limit $k_F \rightarrow 0$, phenomenological analyses of proton scattering data require modifications of the low-density interaction in order to obtain good fits to the data for states with surface-peaked transition densities. These modifications reflect limitations of the LDA. Furthermore, nuclear-matter theories of the effective interaction, such as the Paris-Hamburg (PH) model [34,35], do not necessarily reduce to the free t matrix as $k_F \rightarrow 0$ either [17]. Therefore, although we have chosen the empirical effective interactions which give the best results for the self-conjugacy test, ambiguities in the model of the low-density interaction could affect fitted neutron transition densities.

The sensitivity of transition densities fitted to the 200 MeV data for ^{48}Ca is illustrated in Fig. 7, where the solid lines are based upon the interactions labeled {LR1, LR2, LR3} in Ref. [20] and the dashed lines are based upon interactions {PH1, PH2, PH3} from the same source. The former are based upon the FL t matrix and the latter upon the low-density limit of the PH interaction. Within each set there are three selections of data employed in the analysis, with the PH3 and LR3 interactions being based upon the same and the most complete data set. For the present purposes it is not important to distinguish within the figures between these variations within each set. We find that the spread among results obtained with interactions of the same type is never significantly larger than the uncertainty estimated by the fitting procedure, and is often substantially less. The largest such spread is about $\pm 1.3\delta M_n$ for the 3_2^- state, where δM_n is the estimated uncertainty in M_n.

Systematic differences between the two sets of densities provide an indication of residual uncertainties due to the reaction model. These differences involve both shape and scale. With the exception of the 4_2^+ state, where the two sets agree, the fitted transition radii are

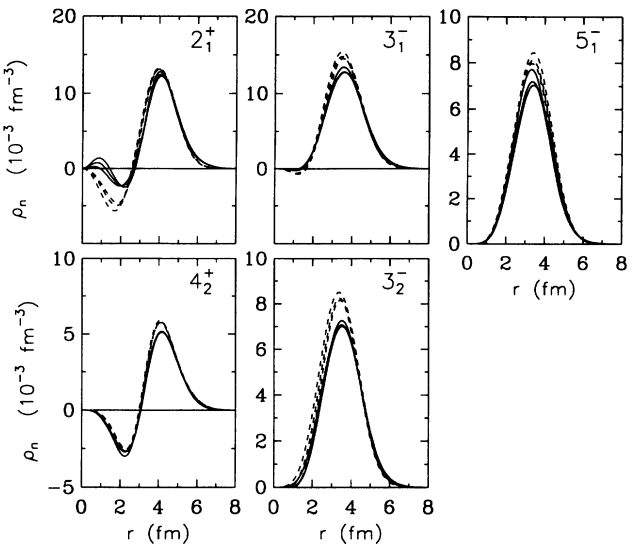

FIG. 7. The sensitivity of ρ_n fitted to 200 MeV data for ^{48}Ca to ambiguities in the low-density effective interaction is illustrated by comparing fits based upon the {PH1, PH2, PH3} interactions (dashed lines) with fits based upon the {LR1, LR2, LR3} interactions (solid lines).

about 0.2 fm smaller for the PH interactions than for the LR interactions. These smaller radii are compensated by larger peak densities, so that the fractional differences between results obtained with the two sets of interactions are generally smaller for integral moments than for densities. Thus, the differences between the LR3 and PH3 interactions, which are both based upon the most complete data set, range between 6% and 18% or $(1.5$–$3)\delta\rho_n$ for the peak of the transition densities or between 3% and 11% or $(0.5$–$3)\delta M_n$ for integral moments. (Note that the deviation between LR3 and PH3 results is not directly related to the estimated uncertainties.) Since the agreement between the densities and moments obtained from the 200 and 318 MeV data are generally as good or better than the agreement between these two sets of interactions for 200 MeV, we conclude that the systematic uncertainties due to the reaction model are probably no more than twice the uncertainties estimated by the fitting procedure. These uncertainties do not affect any important features of the densities or their comparison with theoretical models.

V. ENERGY INDEPENDENCE OF ρ_N

A. Analysis of 200 and 318 MeV data

Neutron transition densities are properties of the target and thus are independent of the properties of the beam. The error bands already include uncertainties due to statistics and normalizations, penetrability and distortion, and incompleteness, but do not include uncertainties due to the effective interactions. As a check that these interaction uncertainties are under control, we can compare densities fitted to data of different energies. We

have taken data for low-lying states of ^{48}Ca at 200 and 318 MeV. If the densities determined separately by each energy's data set are all consistent with each other for each transition, then we can be confident that both the fitted neutron densities and the interactions used to obtain them are indeed accurate.

Neutron transition densities were fitted to data for the 2_1^+, 3_1^-, 3_2^-, 4_2^+, and 5_1^- states of ^{48}Ca at 200 MeV, 318 MeV, and again to both energies simultaneously. Also, the densities fitted at each energy were used in conjunction with the empirical interaction for the other energy to predict the observables at that other energy. For example, the density fitted to 318 MeV data was used with the 200 MeV interaction to calculate the observables for 200 MeV. We call these *cross-energy* calculations.

Finally, in order to simulate typical past analyses, a scale factor fit was done to the combined data set (200 MeV and 318 MeV data) for each state. In the scale factor fit it is assumed that $\rho_n(r) = S\rho_p(r)$, where the proton transition density is held fixed while S is allowed to vary to minimize χ^2. For each case the range of q used in these fits was limited to the dominant peak of the cross section angular distribution so as to sample the bulk of the radial density. Thus, differences between the radial shapes of neutron and proton transition densities are revealed by deviations from the scale factor fits as the momentum transfer increases. These differences are described by the LGE analysis.

The results can be seen in Figs. 8–12. Each figure has the same six-panel format. On data plots, solid lines represent dual-energy fits, short-dashed lines represent single-energy fits, long-dashed lines represent cross-energy calculations, and dotted lines represent scaling fits. The upper right panel in each figure compares fitted densities, where the dashed line is the 200 MeV density, the solid line is the 318 MeV density, and the band is the result of the dual-energy fit. To properly interpret these figures, it must be remembered that the single-energy fits also carry error bands which are somewhat wider than those of the dual-energy fits, particularly for small radii and 318 MeV, but these bands cannot be easily displayed without excessive clutter. To illustrate the sensitivity to shape differences between the proton and neutron transition densities, the lower right panel compares the scaled proton density, shown as a solid line, with the neutron density, shown as a band, that results from the dual-energy analysis.

Before discussing the analysis of each state, we make a few general observations. It can be seen from the figures that the densities determined by the single-energy fits are consistent with the error bands produced by the dual-energy fits. Furthermore, on the data plots, the single-energy fits (dashed lines) are barely distinguishable from the dual-energy fits (solid lines). Similarly, the cross-energy calculations are often difficult to distinguish from the solid lines except at values of q beyond the range analyzed. Note that whenever a cross-energy calculation deviates from the dual-energy fit, the differences are larger for the 200 MeV calculation based upon the 318 MeV density. Because of smaller absorption, the 200 MeV data are more sensitive to details of the radial density. Thus, the dual-energy fits tend to be dominated by the 200 MeV data and to produce densities closest to those fit to the 200 MeV data alone. Nevertheless, these densities provide excellent predictions for the 318 MeV data.

Therefore, even though the angular distributions for each state are rather different for the two energies, essentially the same density results from fits to either energy. This is strong support for the claim that the empirical interactions used in this analysis are accurate and independent of target and that the neutron transition densities fitted using these interactions are accurate to the extent shown by the error bands.

1. 2_1^+ state

The fits to the data for the 2_1^+ state, shown in Fig. 8, are all excellent. It is difficult to distinguish the single-

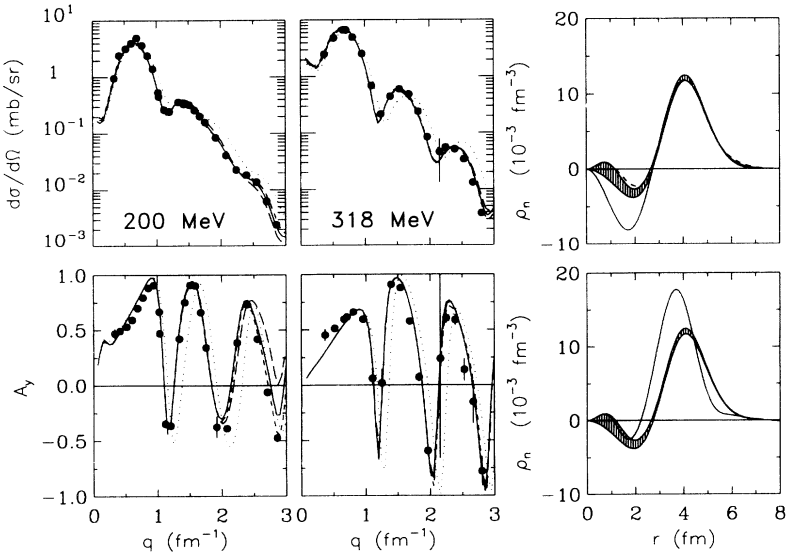

FIG. 8. Results for the 2_1^+ state of ^{48}Ca. In the first two columns, short-dashed lines portray single-energy fits, solid lines dual-energy fits, and long-dashed lines cross-energy calculations, as described in the text. Note that it is difficult to distinguish between these curves. The dotted lines portray dual-energy scale factor fits. In the upper-right panel, the dashed line is the 200 MeV density, the solid line is the 318 MeV density, and the band is the dual-energy density. In the lower-right panel, the band is the dual-energy density and the solid line is the scaled density, $\rho_n = S\rho_p$, based upon the dotted lines in the first two columns.

energy fits (short-dashed lines) from the dual-energy fits (solid lines). Also, the cross-energy calculations (long-dashed lines) are difficult to discern except on the 200 MeV analyzing power plot for $q > 2.8$ fm^{-1}, which is outside the fitting range. Both the cross sections and analyzing powers at both energies are described very well. The resulting densities are shown in the upper right panel. The dashed line is from the fit to the 200 MeV data, the solid line is from the fit to the 318 MeV data, and the band is the density from the combined fit. One has to imagine error bands on the single-energy densities whose widths are somewhat larger than that of the error band shown for the dual-energy density, particularly for small radii and 318 MeV. When this is done, it is easily seen that the three densities are self-consistent.

The scale-factor fit describes the data for the first maxima of the cross section angular distributions well, but the deviations increase rapidly with increasing momentum transfer, revealing a significant difference between the shapes of the neutron and proton transition densities. The lower right panel shows the density of the combined fit as a band and the scaled density as a solid line. The shape of the surface lobe of the scaled proton density is narrower and positioned at smaller r, such that its Fourier transform falls less rapidly with q than that of the LGE density and the corresponding cross section is too large at high q. Nevertheless, the smaller radius for the peak of $S\rho_p(r)$ is compensated by its greater height so that both densities have similar moments and similar form factors at low q, and we find $S \approx M_n/M_p \approx R_{np}$. The LGE analysis clearly permits much more detailed information to be extracted from the data than a simple scale factor, and thus permits more discriminating evaluations of nuclear structure models to be made.

2. 3_1^- state

The fits to the data for the 3_1^- state are shown in Fig. 9. Here again the single-energy fits, the dual-energy fits, and the cross-energy calculations are almost indistinguishable from each other and all provide excellent descriptions of the data, particularly for 200 MeV. The densities in the upper right panel are clearly consistent with each other, with the single-energy fits residing inside the band for most of the plot.

The lower right panel again shows some shape differences between the proton and neutron densities. Even though this is a surface peaked state, the scale factor fits again clearly deviate from the data for large q due in part to the extra height and reduced width of the scaled density.

We have also investigated the likely impact of the unresolved 4_1^+ state on the extraction of the 3_1^- transition density. These states are separated by only 4 keV and could not be resolved by the experiment. However, there is good reason to believe that the strength of the 4_1^+ state is very small compared to that of the 3_1^- state. We will see in Sec. VII that the densities predicted by the ERPA model [4] show excellent agreement with our results. Consequently, we used the ERPA predictions for the 4_1^+ densities in conjunction with our empirical effective interactions to produce predictions for the observables for this state. First, it was found that the observables barely changed when the results of the 4_1^+ calculations were "subtracted" from the 3_1^- data. Second, we refitted the "corrected" 3_1^- data and found that our inability to resolve the minuscule separation of the 4_1^+ and 3_1^- states has very little effect on the densities fitted to either 200 MeV or 318 MeV data. A more detailed description of this analysis is given in Ref. [15].

3. 3_2^- state

The results for the 3_2^- state are shown in Fig. 10. Yet again the single-energy fits and the dual-energy fits are almost indistinguishable from each other and all provide excellent descriptions of the data. Although the 318 MeV density appears to be a little wider than the 200 MeV

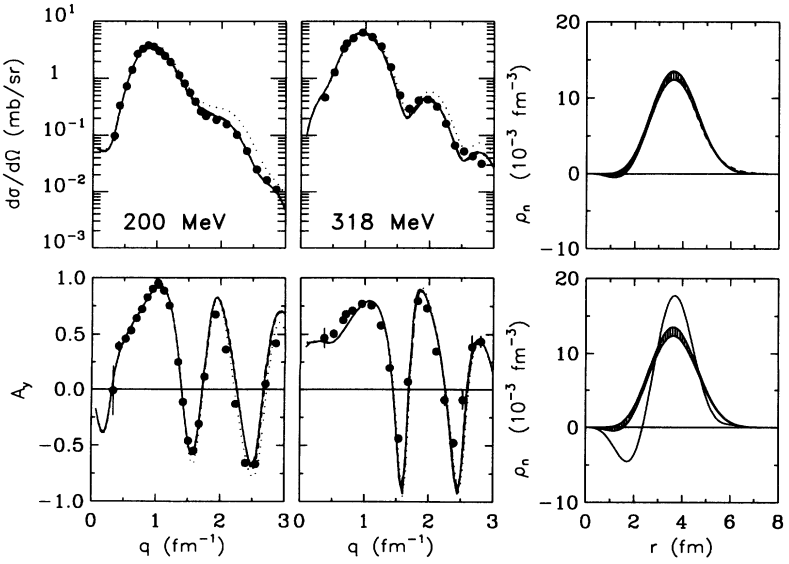

FIG. 9. Results for the 3_1^- state of ^{48}Ca. In the first two columns, short-dashed lines portray single-energy fits, solid lines dual-energy fits, and long-dashed lines cross-energy calculations, as described in the text. Note that it is difficult to distinguish between these curves. The dotted lines portray dual-energy scale factor fits. In the upper-right panel, the dashed line is the 200 MeV density, the solid line is the 318 MeV density, and the band is the dual-energy density. In the lower-right panel, the band is the dual-energy density and the solid line is the scaled density, $\rho_n = S\rho_p$, based upon the dotted lines in the first two columns.

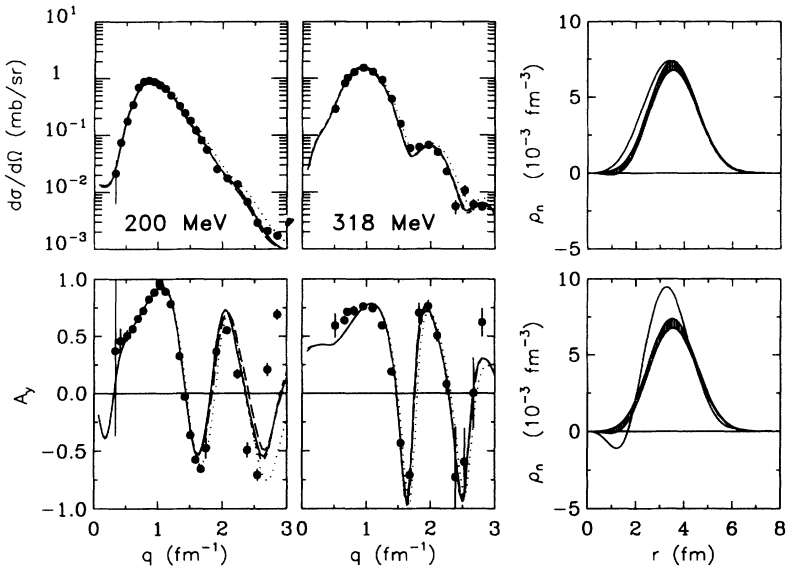

FIG. 10. Results for the 3_2^- state of ^{48}Ca. In the first two columns, short-dashed lines portray single-energy fits, solid lines dual-energy fits, and long-dashed lines cross-energy calculations, as described in the text. Note that it is difficult to distinguish between these curves. The dotted lines portray dual-energy scale factor fits. In the upper-right panel, the dashed line is the 200 MeV density, the solid line is the 318 MeV density, and the band is the dual-energy density. In the lower-right panel, the band is the dual-energy density and the solid line is the scaled density, $\rho_n = S\rho_p$, based upon the dotted lines in the first two columns.

density, the error bands for these two results nearly overlap. Hence, the densities in the upper right panel are essentially self-consistent. The lower right panel shows that the shapes of the neutron and proton densities are similar. As a result of their close similarity, the scale-factor fit does a much better job of reproducing the data than scale fits for the 2_1^+ or the 3_1^- states, but it is still not as accurate at large q as is the LGE fit.

4. 4_2^+ state

As shown in Fig. 11, the single-energy and dual-energy fits and the cross-energy calculations for the 4_2^+ state are again almost indistinguishable from each other and all provide very good descriptions of the data. The single-energy densities plotted in the upper right panel are almost lost in the dual-energy band and hence are inarguably self-consistent.

The lower panel shows the result of the scale-factor fit and demonstrates that the shapes of ρ_n and ρ_p are clearly different. The scale-factor fit does a very poor job of describing the data. The scaled density peaks at smaller r than the LGE density, but the width of the main lobe is greater. Also, the inner lobe is significantly smaller than that of the LGE density. The inward compression in r is again accompanied by an outward stretch of the observables in q.

Note that because the shapes of ρ_n and ρ_p are so different, the fitted scale factor depends strongly upon the range of q that is employed. For the scale-factor analysis shown in Fig. 11 we chose to fit data only for $q < 1.0$ fm^{-1}, which allows the fitted cross section to overshoot the peak of the angular distribution. Had we included data at and beyond the peak in that analysis, we would have obtained a smaller value of S. We chose to restrict the scale-factor analysis to low q so that S would be close to M_n/M_p, which is a long-wavelength or low-q property

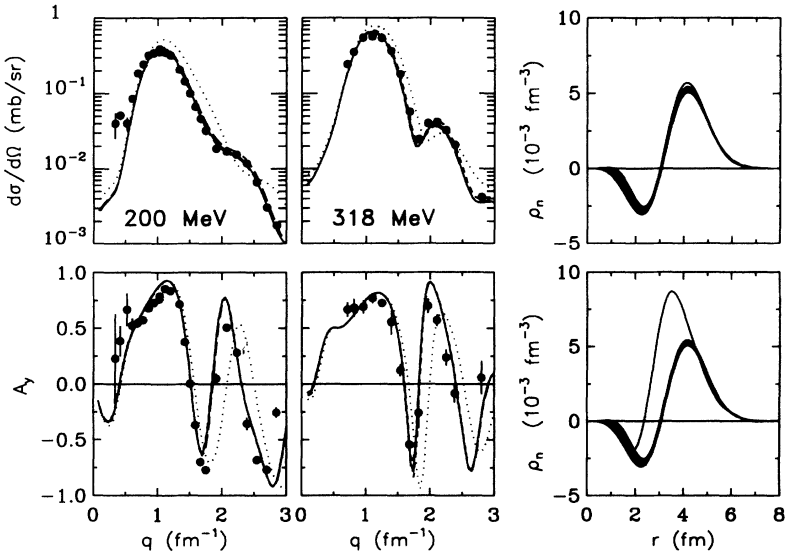

FIG. 11. Results for the 4_2^+ state of ^{48}Ca. In the first two columns, short-dashed lines portray single-energy fits, solid lines dual-energy fits, and long-dashed lines cross-energy calculations, as described in the text. Note that it is difficult to distinguish between these curves. The dotted lines portray dual-energy scale factor fits. In the upper-right panel, the dashed line is the 200 MeV density, the solid line is the 318 MeV density, and the band is the dual-energy density. In the lower-right panel, the band is the dual-energy density and the solid line is the scaled density, $\rho_n = S\rho_p$, based upon the dotted lines in the first two columns.

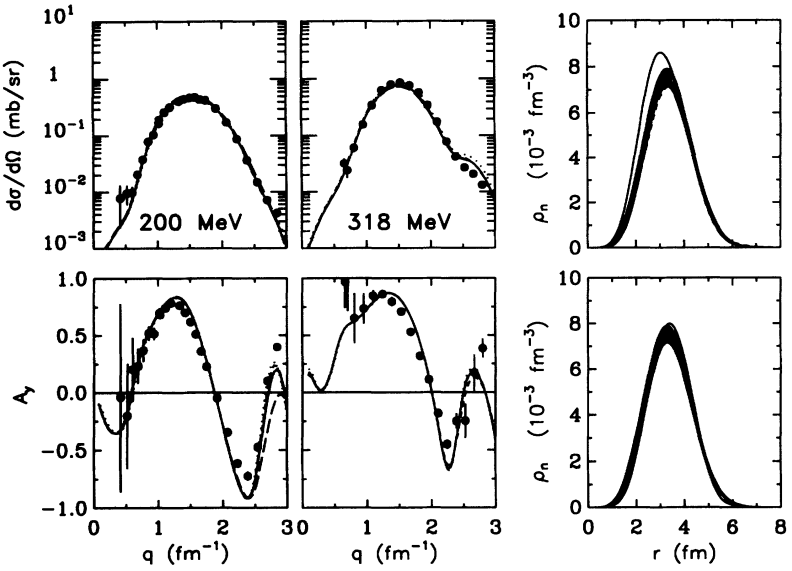

FIG. 12. Results for the 5_1^- state of ^{48}Ca. In the first two columns, short-dashed lines portray single-energy fits, solid lines dual-energy fits, and long-dashed lines cross-energy calculations, as described in the text. Note that it is difficult to distinguish between these curves. The dotted lines portray dual-energy scale factor fits. In the upper-right panel, the dashed line is the 200 MeV density, the solid line is the 318 MeV density, and the band is the dual-energy density. In the lower-right panel, the band is the dual-energy density and the solid line is the scaled density, $\rho_n = S\rho_p$, based upon the dotted lines in the first two columns.

of the transition densities. Obviously, unambiguous values for S can be obtained only when the neutron and proton densities have sufficiently similar shapes. Therefore, the identification of S with M_n/M_p often made in traditional analyses of hadron scattering data can be fraught with difficulties whenever the two densities differ appreciably in shape.

5. 5_1^- state

The results for the 5_1^- state are shown in Fig. 12. The LGE fits, the cross-energy calculations, and the scaling fits are in good agreement with each other and the shapes of ρ_n and ρ_p are just about identical. The curves are a little too high for the 318 MeV cross section for high q and slightly too low near 2.2 fm^{-1} for the 200 MeV analyzing power. While there appears to be a leftward shift of the 318 MeV neutron density, we must remember that the error bands on single-energy fits are wider than on the dual-energy fits, such that the error band for the 318 MeV density nearly overlaps the dual-energy error band. Consequently, there is little or no inconsistency between these results.

B. Comparison with 500 MeV data

We have used our densities in conjunction with the empirical effective interaction for 500 MeV protons [40] to predict cross sections and analyzing powers for the scattering of 500 MeV protons from ^{48}Ca. These calculations are compared to existing data [41] in Fig. 13. In addition, scale-factor fits to low-q data for 500 MeV are shown as dashed lines. Despite the reduced penetrability at 500 MeV, the results for the 2_1^+ data clearly favor the density fitted to the lower-energy (p,p') data over simple proportionality—evidently, useful sensitivity to the shape of the radial density remains at 500 MeV. The differences between the two models are smaller for the 3_1^- state, as also observed at the lower energies.

The data for both states are well reproduced except near the diffraction minima where the calculations predict sharper structures than observed in the data, particularly for the 2_1^+ state. Similar effects were observed by Flanders *et al.* when comparing calculations based upon the empirical effective interaction with 500 MeV data for ^{40}Ca, but to a lesser degree (see Ref. [40]). Corrections due to multiple scattering, angular resolution, and acceptance averaging based upon the quoted experimental conditions do not appear to be sufficient to account for these discrepancies, but the contribution of the 3_1^- state of ^{40}Ca would be sufficient to explain these discrepancies

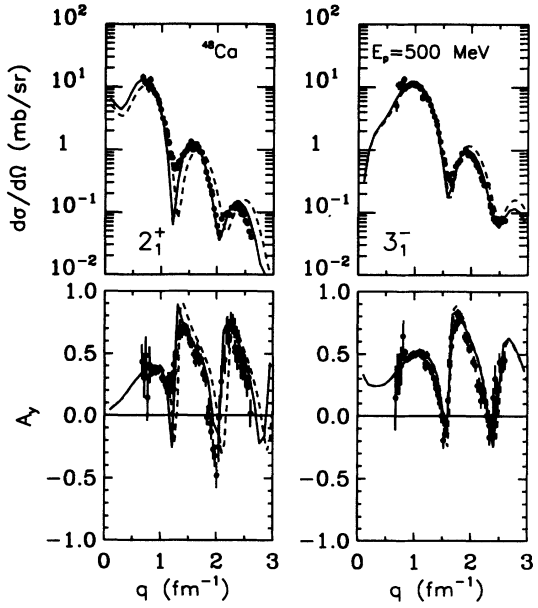

FIG. 13. Predictions for 500 MeV (p,p') (solid lines) based upon fitted neutron densities are compared with data for the 2_1^+ and 3_1^- states of ^{48}Ca. Scale-factor fits to these data are shown by dashed lines.

TABLE II. LGE expansion coefficients for neutron transition densities for ^{48}Ca using $b = 2.0$ fm. The units of a_n are fm^{-3}.

n	2_1^+	3_1^-	3_2^-
1	$(1.53 \pm 0.10) \times 10^{-2}$	$(3.38 \pm 0.13) \times 10^{-2}$	$(1.90 \pm 0.08) \times 10^{-2}$
2	$(-2.35 \pm 0.08) \times 10^{-2}$	$(-1.31 \pm 0.06) \times 10^{-2}$	$(-6.54 \pm 0.25) \times 10^{-3}$
3	$(1.09 \pm 0.03) \times 10^{-2}$	$(1.32 \pm 0.11) \times 10^{-3}$	$(5.31 \pm 0.60) \times 10^{-4}$
4	$(-3.96 \pm 1.96) \times 10^{-4}$	$(3.76 \pm 0.70) \times 10^{-4}$	$(1.99 \pm 0.37) \times 10^{-4}$
5	$(-6.93 \pm 1.61) \times 10^{-4}$	$(-7.95 \pm 2.94) \times 10^{-5}$	$(-3.25 \pm 1.67) \times 10^{-5}$
6	$(-0.93 \pm 1.02) \times 10^{-4}$	$(-3.12 \pm 1.72) \times 10^{-5}$	$(-1.64 \pm 0.96) \times 10^{-5}$
7	$(9.13 \pm 6.75) \times 10^{-5}$	$(3.61 \pm 8.93) \times 10^{-6}$	$(1.04 \pm 5.18) \times 10^{-6}$
8	$(6.09 \pm 4.78) \times 10^{-5}$	$(3.91 \pm 5.67) \times 10^{-6}$	$(1.89 \pm 3.21) \times 10^{-6}$
9	$(1.83 \pm 2.28) \times 10^{-5}$	$(0.95 \pm 2.72) \times 10^{-6}$	$(0.53 \pm 1.43) \times 10^{-6}$
10	$(3.01 \pm 6.80) \times 10^{-6}$	$(0.91 \pm 7.85) \times 10^{-7}$	$(0.66 \pm 3.97) \times 10^{-7}$
11	$(0.24 \pm 1.18) \times 10^{-6}$	$(-0.03 \pm 1.30) \times 10^{-7}$	$(0.19 \pm 6.40) \times 10^{-8}$
12	$(0.33 \pm 9.30) \times 10^{-8}$	$(-1.07 \pm 9.79) \times 10^{-9}$	$(-0.30 \pm 4.73) \times 10^{-9}$
n	4_2^+	5_1^-	
1	$(5.38 \pm 0.30) \times 10^{-3}$	$(9.39 \pm 0.44) \times 10^{-3}$	
2	$(-4.64 \pm 0.14) \times 10^{-3}$	$(-1.59 \pm 0.63) \times 10^{-4}$	
3	$(2.95 \pm 0.48) \times 10^{-4}$	$(-9.56 \pm 3.91) \times 10^{-5}$	
4	$(2.00 \pm 0.37) \times 10^{-4}$	$(-0.22 \pm 1.61) \times 10^{-5}$	
5	$(3.07 \pm 2.17) \times 10^{-5}$	$(2.85 \pm 7.41) \times 10^{-6}$	
6	$(0.13 \pm 1.21) \times 10^{-5}$	$(0.51 \pm 4.18) \times 10^{-6}$	
7	$(-0.19 \pm 6.23) \times 10^{-6}$	$(0.00 \pm 2.24) \times 10^{-6}$	
8	$(-0.01 \pm 2.48) \times 10^{-6}$	$(-0.13 \pm 9.76) \times 10^{-7}$	
9	$(0.04 \pm 7.15) \times 10^{-7}$	$(-0.01 \pm 3.06) \times 10^{-7}$	
10	$(0.00 \pm 1.42) \times 10^{-7}$	$(0.03 \pm 6.53) \times 10^{-8}$	
11	$(-0.02 \pm 1.80) \times 10^{-8}$	$(0.08 \pm 8.72) \times 10^{-9}$	
12	$(-0.03 \pm 1.10) \times 10^{-9}$	$(0.06 \pm 5.63) \times 10^{-10}$	

between theory and experiment for the 2_1^+ state of ^{48}Ca if that impurity has not been subtracted properly in the data analysis by Seth *et al.* [41]. Nevertheless, the fact that the densities fitted to data for 200 and 318 MeV do well at predicting the 500 MeV observables shows that our results are very nearly independent of probe energy.

In addition, neutron densities were fitted to these 500 MeV data with similar results. The resulting densities were consistent with those fitted to the 200 and 318 MeV data when the error bands are taken into consideration [15]. Also, triple-energy fits for the 2_1^+ and 3_1^- states were very successful with the data for 200, 318, and 500 MeV all being very well described by a single fitted neutron density convoluted with three very different effective interactions [15]. This further supports the energy independence of our results.

C. Final results

We have shown that our fitted neutron transition densities are independent of probe energy for all five states. Even the cross-energy calculations are essentially indistinguishable from the dual-energy fits; the occasional small deviations always occur at values of momentum transfer beyond the range analyzed. For each state, the error bands of the single- and dual-energy fitted densities either overlap or are very close. Finally, the dual-energy densities also provide good predictions for independent data at 500 MeV. Therefore, residual errors due to the reaction model appear to be small such that the densities are accurate at the level indicated by the error bands. Hence, the dual-energy fits are taken as the final results of the analysis.

The LGE coefficients for neutron transition densities of ^{48}Ca are listed in Table II. The uncertainties quoted for the LGE expansion coefficients are based upon the diagonal elements of the error matrix, although the full error matrix was used to construct error bands for the densities and to calculate uncertainties in moments of the densities. These diagonal elements are adequate to approximate the fully correlated error envelope for $r < r_m$, but correlations due to the tail bias reduce the uncertainties for $r > r_m$ and consequently result in smaller values for δM_n than can be estimated from the diagonal elements alone [14]. The moments, scale factors, and R_{np} values for the fitted densities are compared with ERPA predictions in Tables III and IV. Although the overall sign of

TABLE III. Comparison of the experimentally (expt) extracted moments, scale factors, and R_{np} with theoretical (th) predictions. Uncertainties in the final digit are given in parentheses. Uncertainties in $M_p^{\rm expt}$ are omitted because ρ_p was held fixed in the fitting procedure.

State	S	$R_{np}^{\rm expt}$	$R_{np}^{\rm th}$	$(\frac{M_n}{M_p})^{\rm expt}$	$(\frac{M_n}{M_p})^{\rm th}$
2_1^+	1.98(5)	1.81(5)	2.02	2.34(5)	2.48
4_2^+	2.18(6)	1.64(5)	3.00	2.03(6)	4.96
3_1^-	1.06(3)	0.97(3)	0.83	1.14(4)	0.84
3_2^-	1.12(4)	1.03(4)	0.95	1.13(4)	1.14
5_1^-	0.86(4)	0.81(4)	0.44	0.96(8)	0.52

TABLE IV. Comparison of the experimentally (expt) extracted moments with theoretical (th) predictions. The units for M_n, M_p, M_0, and M_1 are fm^L for multipolarity L. Uncertainties in the final digit are given in parentheses. Uncertainties in $M_p^{\rm expt}$ are omitted because ρ_p was held fixed in the fitting procedure.

State	$M_n^{\rm expt}$	$M_n^{\rm th}$	$M_p^{\rm expt}$	$M_p^{\rm th}$	$M_0^{\rm expt}$	$M_0^{\rm th}$	$M_1^{\rm expt}$	$M_1^{\rm th}$
2_1^+	9.46(21)	9.90	4.04	4.00	13.50(21)	13.90	5.42(21)	5.90
4_2^+	100.0(32)	125.1	49.25	25.20	149.3(32)	150.3	50.8(32)	99.9
3_1^-	36.3(12)	39.23	31.78	46.79	68.1(12)	86.02	4.5(12)	−7.56
3_2^-	18.36(57)	17.77	16.23	15.54	34.59(57)	33.31	2.13(57)	2.23
5_1^-	315.(26)	276.4	328.5	528.0	644.(26)	804.4	−14.(26)	−251.6

ρ_0 is arbitrary, we have chosen $M_p > 0$ for all states, such that the sign of M_n is determined by the relative sign between ρ_n and ρ_p. For most states we find that the three measures of the relative contributions of neutrons and protons, viz., S, R_{np}, and M_n/M_p, are in good agreement with each other, but appreciable differences between these quantities are found for states with significant shape differences between ρ_n and ρ_p, such as the 2_1^+ and 4_2^+ states. The comparison between experiment and theory is discussed in Sec. VII.

VI. COMPARISON WITH PREVIOUS ANALYSES

Our results for moments of the neutron and proton transition densities are compared with the results from several previous analyses of pion, alpha, or proton scattering from ^{48}Ca in Table V. These comparisons are of interest particularly for the 2_1^+ state of ^{48}Ca because the M_n/M_p ratio for this state has been identified by Bernstein *et al.* [8] as unusually large for a lowest 2^+ excitation. Using a value of M_0 deduced by Bernstein [42] from the alpha scattering data of Ref. [43] for $E_\alpha = 31$ MeV and a value of M_p deduced from the low-q electron scattering results of Eisenstein *et al.* [44], Ref. [8] reports a value of $M_n/M_p = 3.28(40)$ which is more than 2σ greater than our value. These old alpha and electron scattering experiments were both analyzed using collective models. However, it has been established that the Bernstein prescription [42] suffers from ambiguities in the choice of radius and must be calibrated for each multipolarity using known transitions in nearby nuclei [45,46]. A more careful determination of the radius might bring the alpha scattering result into closer agreement with ours.

TABLE V. Comparison of results to previous analyses of ^{48}Ca. The laboratory kinetic energies (K) are given in MeV. The uncertainty of the last significant figure is given in parentheses.

Method	K	$2_1^+ \frac{M_n}{M_p}$	$3_1^- \frac{M_n}{M_p}$
(p,p') [a]	200, 318	2.34(5)	1.14(4)
$(\pi^\pm,\pi^\pm)$ [b]	180	2.63(37)	1.17(14)
$(\pi^\pm,\pi^\pm)$ [c]	180	2.38(33)	1.14(14)
(p,p') [d]	800	3.2(5)	
(α,α') [e]	31	3.28(40)	

[a]Present result based upon LGE fits to ρ_n combined with ρ_p from Ref. [37].
[b]Scaling result from Ref. [48].
[c]Collective result from Ref. [48].
[d]Collective result from Ref. [47].
[e]Collective result from Ref. [8].

Similarly, measurements of M_n for ^{48}Ca were performed by Adams *et al.* [47] using 800 MeV protons. They fit $\rho_n(r)$ to (p,p') data in a distorted wave impulse approximation (DWIA) analysis using the same Tassie parametrization used by Eisenstein *et al.* Their value for M_n/M_p for the 2_1^+ state is 3.2(5), which is also about 2σ greater than ours. Comparable results using 500 MeV protons were obtained by Ref. [41] using a collective model analysis. However, we find that the transition densities fitted to proton scattering at 200 and 318 MeV describe the 500 MeV data very well, demonstrating that our densities are consistent with the higher-energy data despite the apparent discrepancy with those collective model analyses, which do not necessarily yield unambiguous results for M_n/M_p. In fact, Adams *et al.* [47] quote a value of $R_{np} = 2.6$ for the Tassie model that is in much better agreement with our M_n/M_p and they suggest that R_{np} is a better estimate of the relative contributions of neutrons and protons than M_n/M_p. Also, we note that their analysis was based upon the low-q (e,e') data of Eisenstein *et al.* [44], which did not reach the peak of the form factor, whereas the (p,p') data only barely extended down to the peak of the angular distribution.

Finally, proton and neutron matrix elements for the 2_1^+ and 3_1^- states of ^{48}Ca were deduced from data for the scattering of 180 MeV pions by Boyer *et al.* [48]. The model dependence of their results was checked by performing both collective model calculations and scaling fits based upon a Tassie model fitted by Ref. [44] to low momentum transfer (e,e') data. Their M_p results are consistent with electromagnetic measurements. Their M_n/M_p results for the ^{48}Ca 2_1^+ state are 2.63(37) and 2.38(33) using the scaling model and the collective model, respectively. The latter value agrees favorably with our value of 2.34(5). Their M_n/M_p results for the ^{48}Ca 3_1^- state are 1.17(14) and 1.14(14) for the scaling and collective model, respectively. These results also compare quite favorably to our value of 1.14(4). Although pion scattering also suffers from strong absorption, the internal consistency provided by measurements for both π^+ and π^- helps to reduce the model dependence of the values deduced for M_n/M_p. Therefore, we conclude that the evidence for a very large value of $M_n/M_p \approx 3.2$ for

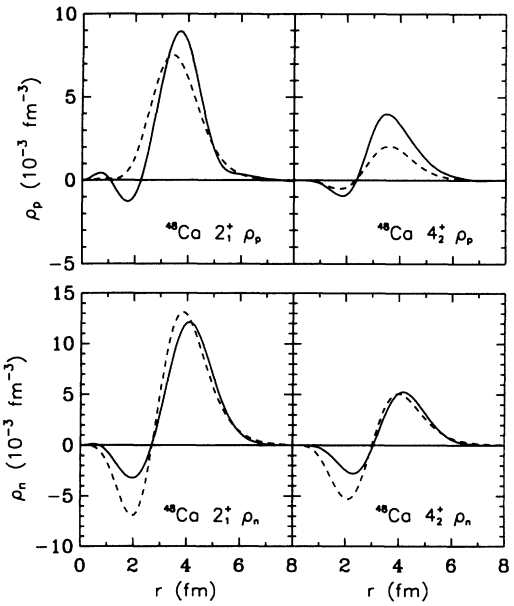

FIG. 14. ERPA predictions (dashed lines) are compared with experimental proton and neutron transition densities (solid lines) for positive parity states of ^{48}Ca.

the lowest 2^+ state of ^{48}Ca is fairly weak, and that more reliable analyses suggest a value of $M_n/M_p \approx 2.3$ which is still larger than for most 2_1^+ states [8], but not remarkably so.

VII. COMPARISON TO ERPA CALCULATIONS

The predictions of the ERPA theory [4] for ^{48}Ca proton and neutron transition densities for positive and negative parity are shown in Figs. 14 and 15, respectively. The solid lines are experimental results and the dashed lines are the ERPA predictions. The peak of the ERPA 2_1^+ proton density is about 15% smaller and occurs about 0.3 fm inside the peak of the measured density, whereas the predicted and measured neutron densities are very similar. Similarly, the neutron density predicted for the 4_2^+ state is in good qualitative agreement with the measured density for $r > 3$ fm, but even though the shape of ERPA proton density is approximately correct its strength is too small by about a factor of 2. The calculated densities for the 3_1^- state both agree with the data very well. The ERPA 3_2^- proton density agrees well with experiment, whereas the theoretical neutron density is smaller and narrower than measured. Finally, the prediction for the 5_1^- proton density is good, but the predicted neutron density is only about half as strong as the measured density.

For each of the positive parity states we observe that the prediction for the neutron density is better than for the proton density. In contrast, for each of the negative parity states, the prediction for the proton density is better than for the neutron density. While some of the differences mentioned here are small, the trends for the positive and negative parity states are very systematic and the effects are quite pronounced for the 3_2^-, 4_2^+, and 5_1^- states. Similar trends can be observed in the comparisons between theoretical and experimental moments given in Tables III and IV. For example, the theoretical and experimental values for M_n/M_p are in good agreement for the 2_1^+, 3_1^-, and 3_2^- states, but for the 4_2^+ state the prediction for M_n/M_p is about a factor of 2.5 too large whereas for the 5_1^- state it is almost a factor of 2 too small. We also find that although the ERPA predictions are fairly accurate for M_0, several of the M_1 predictions are much too large, especially for the 5_1^- state. A qualitative interpretation of these comparisons can be made by considering the properties of the ERPA model.

In the shell model, if we consider only $1p1h$ transitions

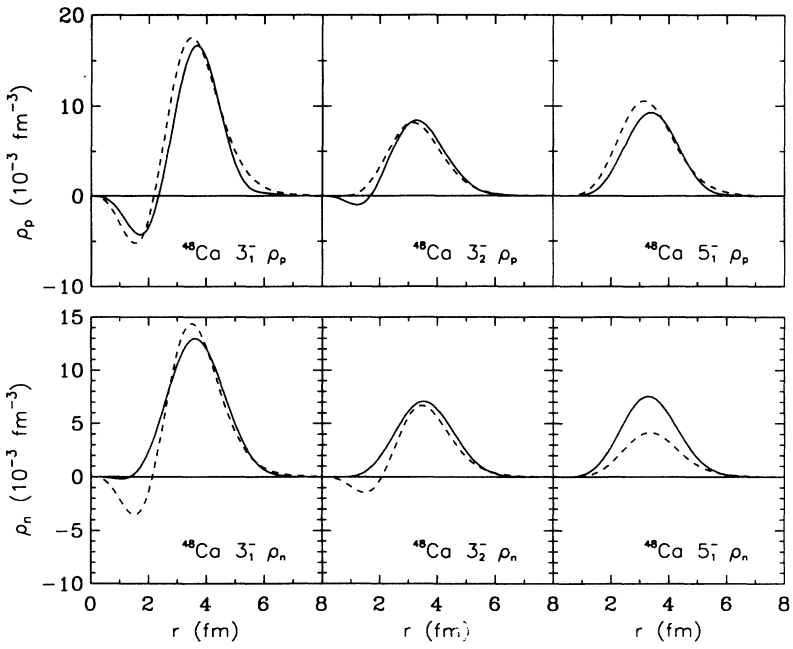

FIG. 15. ERPA predictions (dashed lines) are compared with experimental proton and neutron transition densities (solid lines) for negative parity states of ^{48}Ca.

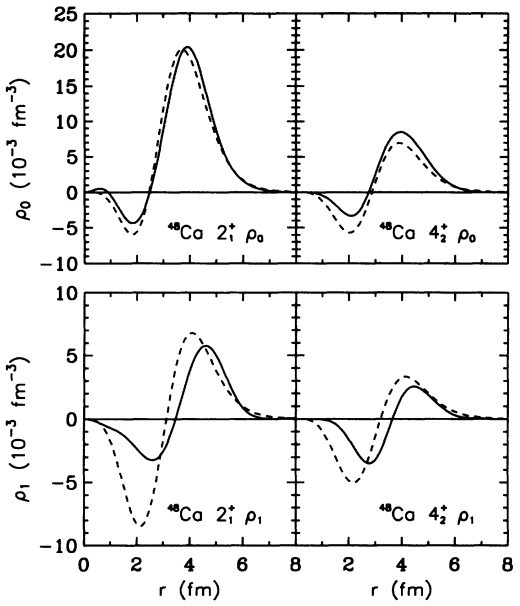

FIG. 16. ERPA predictions (dashed lines) are compared with experimental isoscalar and isovector transition densities (solid lines) for positive parity states of ^{48}Ca.

from valence orbitals to orbitals that are just above the Fermi surface, we can see that low-lying positive parity states can be formed only by transitions from the neutron $1f_{7/2}$ to the $2p_{3/2}$, $2p_{1/2}$, and $1f_{5/2}$ orbitals. Similarly, the $1p1h$ components of negative parity states are formed primarily by proton transitions from the almost degenerate $1d_{3/2}$ and $2s_{1/2}$ levels to the $1f_{7/2}$ level. Thus, for positive parity states the proton transition density is largely composed of $2p2h$ configurations linked to the dominant $1p1h$ neutron configuration by the residual interaction, whereas for negative parity states the neutron transition density arises from higher-order contributions. These core polarization effects are included in the ERPA model through $2p2h$ configurations. Thus, the ERPA model is able to predict the transition strengths without using adjustable effective charges. However, if the $2p2h$ contributions are too small, we would expect the proton (neutron) transition density to be too weak for states of positive (negative) parity.

These effects can also be illustrated by comparing theoretical and experimental densities in isoscalar and isovector form, as shown in Figs. 16 and 17, where $\rho_0 = \rho_n + \rho_p$ and $\rho_1 = \rho_n - \rho_p$. Good agreement between theory and experiment is obtained for the isoscalar transition densities, but most of the predicted isovector transition densities are too strong even though their shapes are in fairly good qualitative agreement with experiment. These trends support the conclusion that isoscalar $2p2h$ contributions need to be stronger than predicted by the ERPA model and that isovector contributions must be damped.

VIII. SUMMARY AND CONCLUSIONS

New cross section and analyzing power data for ^{48}Ca(p,p') have been acquired at 200 and 318 MeV for states up to approximately 7 MeV in excitation energy and for momentum transfers between about 0.4 and 3.0 fm^{-1}.

We have fitted neutron transition densities for the 2_1^+ (3.832 MeV), 3_1^- (4.507 MeV), 3_2^- (5.370 MeV), 4_2^+ (6.342 MeV), and 5_1^- (5.729 MeV) states using accurate target-independent empirical effective interactions that were fitted to proton scattering data for self-conjugate targets. We have demonstrated that ambiguities in the isoscalar components of the empirical effective interactions have relatively little effect upon the fitted densities. Similarly,

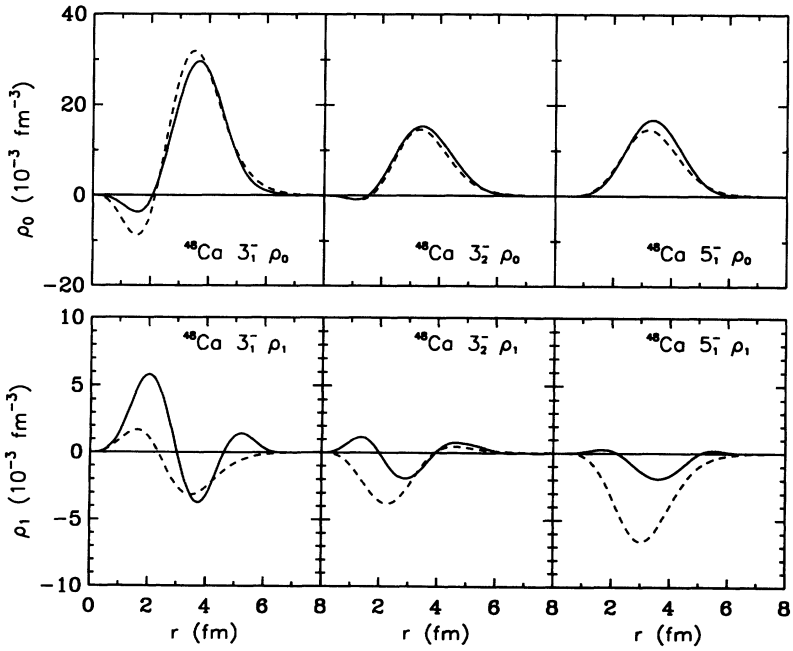

FIG. 17. ERPA predictions (dashed lines) are compared with experimental isoscalar and isovector transition densities (solid lines) for negative parity states of ^{48}Ca.

uncertainties in the isovector interaction, for which empirical calibrations are unavailable, do not affect the fitted densities. Although systematic uncertainties due to residual errors in the effective interaction remain about twice as large as the uncertainties estimated by the fitting procedure for single-energy analyses, these uncertainties do not affect any of the important characteristics of the results or the comparison between theory and experiment. Dual-energy fits were compared to single-energy fits and to cross-energy calculations for 200 and 318 MeV. It was found that for each state these fitted neutron transition densities were self-consistent to the level indicated by the error bands, confirming the accuracy of the results. Also, we showed that the extracted densities provide excellent predictions of the 500 MeV proton scattering data for the 2_1^+ and 3_1^- states. Therefore, the energy independence of the fitted densities demonstrates that the reaction model for these energies is sufficiently accurate to unfold a unique density for each state despite appreciable differences between the angular distributions for these energies.

For several states, the shapes of the proton and neutron transition densities are sufficiently different that scale factor fits fail to provide adequate fits beyond the first peak of the angular distributions. Nevertheless, the data for these states are described very well when the radial densities are fitted. These observations demonstrate that proton scattering in the 200–318 MeV energy range exhibits good sensitivity to the radial shape of the neutron transition density. We also observe in the cross-energy calculations that the 200 MeV data are more sensitive than the 318 MeV data to details of the radial density.

Calculations due to Brand, Allaart, and Dickhoff [4] based upon the extended random phase approximation (ERPA) are in good agreement with most of the densities considered here. However, the ERPA predictions for ^{48}Ca tend to be better for the proton densities of negative parity states and better for the neutron densities of positive parity states. We also find that the ERPA model provides good predictions for isoscalar densities, but that its predictions for isovector transition densities are too strong for the low-lying states. This pattern can be attributed to the fact that the densities for which the ERPA excels are the same as those that can be described by single-particle transitions from the valence orbitals to the lowest orbitals above the Fermi level. For these densities, the $2p2h$ contributions are merely a correction while for the others they are dominant. Although inclusion of $2p2h$ contributions stabilizes the low-lying RPA excitations and provides qualitatively correct predictions for both the shape and strength of these transition densities, some improvement in the model of short-range correlations is probably required. Also, calculating the second-order single-particle propagator exactly should yield a more accurate estimate of the $2p2h$ contributions.

Accurate proton transition densities have long been available from electron scattering measurements and have provided invaluable insights into nuclear structure, but comparable information for neutron transition densities has been unavailable until recently. Although the scattering of intermediate energy protons has good intrinsic radial sensitivity, extraction of accurate neutron transition densities requires the use of empirically calibrated effective interactions. Since neutron transition densities should be probe independent, our demonstration of the energy independence of extracted densities confirms the accuracy of the analysis procedures. Therefore, accurate and reliable neutron transition densities can now be extracted from proton scattering data and there is good reason to expect that this detailed information, especially in conjunction with complementary information from electron scattering, will provide many important insights into nuclear structure.

ACKNOWLEDGMENTS

We thank Prof. W. H. Dickhoff for tables of the ERPA transition densities and W. Loszowski of IUCF for assistance with the targets. This work was supported in part by grants from the National Science Foundation and the U.S. Department of Energy. Two of the authors (P.B. and H.S.) acknowledge National Research Council-NASA/GSFC Research Associateships held at the time of publication.

[1] J. E. Wise, J. S. McCarthy, R. Altemus, B. E. Norum, R. R. Whitney, J. Heisenberg, J. Dawson, and O. Schwentker, Phys. Rev. C **31**, 1699 (1985).
[2] P. H. Karen, Ph.D. thesis, University of Virginia, 1993.
[3] M. G. E. Brand, K. Allaart, and W. H. Dickhoff, Phys. Lett. B **214**, 483 (1988).
[4] M. G. E. Brand, K. Allaart, and W. H. Dickhoff, Nucl. Phys. **A509**, 1 (1990).
[5] J. Heisenberg, Adv. Nucl. Phys. **12**, 61 (1981).
[6] J. Heisenberg and H. P. Blok, Annu. Rev. Nucl. Part. Sci. **33**, 569 (1983).
[7] A. M. Bernstein, V. R. Brown, and V. A. Madsen, Phys. Rev. Lett. **42**, 425 (1979).
[8] A. M. Bernstein, V. R. Brown, and V. A. Madsen, Phys. Lett. **103B**, 255 (1981).
[9] A. M. Bernstein, V. R. Brown, and V. A. Madsen, Comments Nucl. Part. Phys. **11**, 203 (1983).
[10] J. J. Kelly, Phys. Rev. C **37**, 520 (1988); J. A. Carr, F. Petrovich, and J. Kelly, in *Neutron-Nucleus Collisions—A Probe of Nuclear Structure* (*Burr Oak State Park, Glouster, Ohio*), Proceedings of the Conference on Neutron-Nucleus Collisions—A Probe of Nuclear Structure, edited by J. Rapaport, R. W. Finlay, S. M. Grimes, and F. Dietrich, AIP Conf. Proc. No. 124 (AIP, New York, 1984), p. 230.
[11] J. J. Kelly, W. Bertozzi, T. N. Buti, J. M. Finn, F. W.

Hersman, M. V. Hynes, C. Hyde-Wright, B. E. Norum, A. D. Bacher, G. T. Emery, C. C. Foster, W. P. Jones, D. W. Miller, B. L. Berman, J. A. Carr, and F. Petrovich, Phys. Lett. **169B**, 157 (1986).

[12] J. J. Kelly, Q. Chen, P. P. Singh, M. C. Radhakrishna, W. P. Jones, and H. Nann, Phys. Rev. C **41**, 2525 (1990).

[13] J. J. Kelly, M. A. Khandaker, P. Boberg, A. E. Feldman, B. S. Flanders, S. Hyman, H. Seifert, P. Karen, B. E. Norum, P. Welch, S. Nanda, and A. Saha, Phys. Rev. C **44**, 1963 (1991).

[14] M. A. Khandaker, J. J. Kelly, P. Boberg, A. E. Feldman, B. S. Flanders, S. Hyman, H. Seifert, P. Karen, B. E. Norum, P. Welch, S. Nanda, and A. Saha, Phys. Rev. C **44**, 1978 (1991).

[15] A. E. Feldman, P. Boberg, B. S. Flanders, S. D. Hyman, J. J. Kelly, M. A. Khandaker, H. Seifert, P. Karen, B. E. Norum, P. Welch, A. Saha, S. Nanda, Q. Chen, and A. Scott, Bull. Am. Phys. Soc. **35**, 1038 (1990); A. E. Feldman, Ph.D. thesis, University of Maryland, 1991.

[16] J. J. Kelly, B. S. Flanders, F. W. Hersman, J. H. Heisenberg, J. Calarco, J. P. Connelly, T. E. Millimen, A. Scott, F. T. Baker, V. Penumetcha, W. P. Jones, G. T. Emery, A. D. Bacher, C. Olmer, M. A. Grimm, and M. L. Whiten, Phys. Rev. C **47**, 2146 (1993).

[17] J. J. Kelly, W. Bertozzi, T. N. Buti, J. M. Finn, F. W. Hersman, C. Hyde-Wright, M. V. Hynes, M. A. Kovash, B. Murdock, B. E. Norum, B. Pugh, F. N. Rad, A. D. Bacher, G. T. Emery, C. C. Foster, W. P. Jones, D. W. Miller, B. L. Berman, W. G. Love, J. A. Carr, and F. Petrovich, Phys. Rev. C **39**, 1222 (1989).

[18] J. J. Kelly, Phys. Rev. C **39**, 2120 (1989).

[19] H. Seifert, Ph.D. thesis, University of Maryland, 1990.

[20] H. Seifert, J. J. Kelly, A. E. Feldman, B. S. Flanders, M. A. Khandaker, Q. Chen, A. D. Bacher, G. P. A. Berg, E. J. Stephenson, P. Karen, B. E. Norum, P. Welch, and A. Scott, Phys. Rev. C **47**, 1615 (1993).

[21] See AIP document no. PAPS PRVCA-49-2068-31 for 31 pages containing a complete tabulation of the data described in this paper. Order by PAPS number and journal reference from the American Institute of Physics, Physics Auxiliary Publication Service, 500 Sunnyside Boulevard, Woodbury, New York 11797-2999. The price is $1.50 for each microfiche (60 pages) or $5.00 for photocopies of up to 30 pages, and $0.15 for each additional page over 30 pages. Airmail additional. Make checks payable to the American Institute of Physics.

[22] J. R. Breene, Nucl. Data Sheets **23**, 1 (1987).

[23] Y. Fujita, M. Fujiwara, S. Morinobu, T. Yamazaki, T. Itahashi, H. Ikegami, and S. I. Hayakawa, Phys. Rev. C **37**, 45 (1988).

[24] R. A. Arndt, program SAID (unpublished); R. A. Arndt, L. D. Roper, R. A. Bryan, R. B. Clark, B. J. VerWest, and P. Signell, Phys. Rev. D **28**, 97 (1983).

[25] M. W. McNaughton, Los Alamos Scientific Laboratory Report No. LA-8307, 1980 (unpublished).

[26] I. G. Atencio, J. F. Amann, R. L. Boudrie, and C. L. Morris, Nucl. Instrum. Methods **187**, 318 (1981).

[27] J. J. Kelly, computer program ALLFIT (unpublished).

[28] J. J. Kelly, P. Boberg, A. E. Feldman, B. S. Flanders, M. A. Khandaker, S. D. Hyman, H. Seifert, P. Karen, B. E. Norum, P. Welch, S. Nanda, and A. Saha, Phys. Rev. C **44**, 2602 (1991).

[29] J. J. Kelly, computer program LEA (unpublished).

[30] F. Petrovich, H. McManus, V. A. Madsen, and J. Atkinson, Phys. Rev. Lett. **22**, 895 (1969).

[31] T. Cheon, K. Takayanagi, and K. Yazaki, Nucl. Phys. **A437**, 301 (1985); **A445**, 227 (1985).

[32] J. J. Kelly, A. E. Feldman, B. S. Flanders, H. Seifert, D. Lopiano, B. Aas, A. Azizi, G. Igo, G. Weston, C. Whitten, A. Wong, M. V. Hynes, J. McClelland, W. Bertozzi, J. M. Finn, C. E. Hyde-Wright, R. W. Lourie, P. E. Ulmer, B. E. Norum, and B. L. Berman, Phys. Rev. C **43**, 1272 (1991).

[33] M. A. Franey and W. G. Love, Phys. Rev. C **31**, 488 (1985).

[34] H. V. von Geramb, in *The Interaction Between Medium Energy Nucleons in Nuclei* (*Indiana Cyclotron Facility, Bloomington, Indiana*), Proceedings of the Workshop on the Interactions Between Medium Energy Nucleons in Nuclei, edited by H. O. Meyer, AIP Conf. Proc. No. 97 (AIP, New York, 1982), p. 44.

[35] L. Rikus, K. Nakano, and H. V. von Geramb, Nucl. Phys. **A414**, 413 (1984).

[36] L. Ray, Phys. Rev. C **41**, 2816 (1990).

[37] H. de Vries, C. S. de Jager, and C. de Vries, At. Data Nucl. Data Tables **36**, 495 (1987).

[38] L. Ray and G. W. Hoffmann, Phys. Rev. C **31**, 538 (1985); L. Ray (private communication).

[39] R. A. Miskimen, Ph.D. thesis, Massachusetts Institute of Technology, 1983.

[40] B. S. Flanders, J. J. Kelly, H. Seifert, D. Lopiano, B. Aas, A. Azizi, G. Igo, G. Weston, C. Whitten, A. Wong, M. V. Hynes, J. McClelland, W. Bertozzi, J. M. Finn, C. E. Hyde-Wright, R. W. Lourie, B. E. Norum, P. E. Ulmer, and B. L. Berman, Phys. Rev. C **43**, 2103 (1991).

[41] K. K. Seth, D. Barlow, A. Saha, R. Soundranayagam, S. Iversen, M. Kaletka, M. Basko, D. Smith, G. W. Hoffmann, M. L. Barlett, R. Fergerson, J. McGill, and E. C. Milner, Phys. Lett. **158B**, 23 (1985).

[42] A. M. Bernstein, Adv. Nucl. Phys. **3**, 325 (1969).

[43] E. P. Lippincott and A. M Bernstein, Phys. Rev. **163**, 1170 (1967).

[44] R. A. Eisenstein, D. W. Madsen, H. Thiessen, L. S. Cardman, and C. K. Bockelman, Phys. Rev. **188**, 1815 (1969).

[45] H. Rebel, Z. Phys. A **277**, 35 (1976); H. Rebel, R. Pesl, H. J. Gils, and E. Friedman, Nucl. Phys. **A368**, 61 (1981).

[46] G. J. Wagner, P. Grabmayr, and H. R. Schmidt, Phys. Lett. **113B**, 447 (1982).

[47] G. S. Adams, T. S. Bauer, G. Igo, G. Pauletta, C. A. Whitten, Jr., A. Wriekat, G. W. Hoffmann, G. R. Smith, and M. Gazzaly, Phys. Rev. C **21**, 2485 (1980).

[48] K. G. Boyer, W. B. Cottingame, L. E. Smith, S. J. Greene, C. F. Moore, J. S. McCarthy, R. C. Minehart, J. F. Davis, G. R. Burelson, G. S. Blanpied, C. A. Goulding, H. A. Thiessen, and C. L. Morris, Phys. Rev. C **24**, 598 (1981).